Greenhouse gas effects on Quaternary climates

Mathis P Hain[a] **and Thomas B Chalk**[b], [a]University of California Santa Cruz, Earth and Planetary Sciences, Santa Cruz, CA, United States; [b]Aix-Marseille Université, CNRS, IRD, INRAE, CEREGE, Europôle Méditerranéen de l'Arbois, Aix-en-Provence Cedex, France

Abstract

Slight but regular changes in Earth's orbit paced the rhythm of recurring ice age climate cycles that define the Quaternary period, and from detailed reconstructions we now understand that many of these changes were mediated by climate/carbon cycle feedbacks that changed the concentration of greenhouse gasses (GHGs) in the atmosphere to warm and cool the planet. Among the various GHGs the strongest effect came from changing atmospheric carbon dioxide (CO_2), as supported by an expanding body of available reconstructions. Reconciling the orbital and CO_2 theory is an open challenge for researchers of Quaternary climate change, and a significant opportunity to improve projections of future carbon cycle feedbacks in response to anthropogenic climate change.

Keywords

Carbon cycle feedbacks; Carbon dioxide; CO_2; Energy balance; Greenhouse effect; Greenhouse gas climate forcing; Greenhouse gas reconstruction; Greenhouse gasses; Methane; Mid-Pleistocene Transition; Nitrous oxide; Northern hemisphere glaciation; Orbital theory; Quaternary climate

Key points

- Part 1 summarizes the role of the greenhouse effect in the Earth System.
- Part 2 surveys reconstructions of CO_2 and other greenhouse gasses.
- Part 3 reviews hypotheses on the role of CO_2 in shaping Quaternary climates.

Introduction—The greenhouse effect

When our Sun shines on a greenhouse here on Earth the energy contained in its sunlight heats up the soil, plants and water inside but the glass prevents the warm air and moisture from escaping. Just as our greenhouse warms up at sunrise it cools down as the sun sets, because it radiates more heat into the environment once hot. The effect of water in this system is twofold: heating and evaporating water requires a great deal of energy input so as to slow down the heating and cooling of the greenhouse through the cycle of the day, but the water vapor also traps the heat radiated by soil and plants akin to the effect of the glass. If you set a dry and a

wet glass jar into the midday sun, the dry one heats up quicker but the wet one gets hotter–because the water vapor acts as a heat-trapping greenhouse gas (GHG). These same concepts also apply to our Earth as a whole, with the daily cycle remaining similar from week-to-week and year-to-year but changing season-to-season and over millennia along with Earth's orbit around the Sun. All these factors act together to yield the variable climates on Earth.

Earth's energy balance and surface temperature

Nuclear fusion reactions within the Sun produce about 383 million billion billion Joules of thermal energy every second (383×10^{24} W; S_0), but that heat cannot be moved (conducted or advected) away though space and thus accumulates to heat up the Sun to make it glow, shine and burn—the emission of sunlight includes long-wave thermal radiation that we feel when we face it, short-wave radiation that is visible to our eyes, as well as ultra-violet (UV) radiation that gives sunburn. Earth circles the Sun at a distance of about 150 billion meters (1 AU; d_{SE}) and intercepts a tiny fraction of total sunlight, proportional to the ratio of Earth's cross-section area (A_{cs}) to the area of the sphere centered on the Sun and extending to Earth's orbit. Hence, Earth receives a total radiative energy flux (R_{solar}) of about 173 million billion Joules per second (173×10^{15} W = 173 PW), which corresponds to an average of 341 W per square meter of Earth surface:

$$R_{solar} = S_0 \cdot \frac{A_{cs}}{A_d} = 173PW = 341\frac{W}{m^2} \cdot A_s = R_{absorbed} + R_{reflected} \quad (1a)$$

$$R_{absorbed} = (1 - \alpha) \cdot R_{solar} \quad (1b)$$

The three types of solar radiation have different fates when reaching Earth (Fig. 1, yellow arrows): (1) almost all of the UV light is absorbed by the ozone layer in Earth's stratosphere, never to reach the surface, (2) visible light passes through air but much of it is scattered and reflected back to space by water droplets, ice and dust, never to be absorbed by Earth, and (3) a portion of thermal radiation passes through the atmosphere to heat up Earth's surface while the majority of the Sun's long-wave radiation excites vibrations of air molecules hence absorbing the incoming radiation, which therefore never reaches the surface. That is, in net, 30% of sunlight is reflected (albedo; α=0.3), 23% is absorbed by and heats-up the atmosphere, and 47% is absorbed by and heats-up the solid Earth surface, respectively corresponding to total fluxes of 52PW, 40PW and 81PW, or specific fluxes averaged over the entire Earth surface area (A_s) of 102 W/m^2, 78 W/m^2 and 161 W/m^2 (Trenberth et al., 2009).

Other natural energy sources to Earth include geothermal heating from the Earth interior (about 46TW, 0.1 W/m^2), the potential energy of space particles absorbed by Earth (0.6 GW, ~0 W/m^2) and gas-loss to space (>0.4 GW, ~0 W/m^2). Estimates of contemporary heating from primary energy use from fossil fuel and nuclear sources by humans is about 17 TW (0.03 W/m^2) or about one third of the natural geothermal heat flux, and thus heating by Sun today (239 W/m^2 absorption by atmosphere and surface) is about 1800-times higher than heating from below (0.13 W/m^2). At a global mean temperature (GMT) of 13.9 °C for the 20th century the Earth surface transfers 97 W/m^2 of heat to surface air and emits 396 W/m^2 long-wave radiation upwards, of which only about 22 W/m^2 reaches space directly while 374 W/m^2 is absorbed by clouds and greenhouse gasses (Fig. 1; surface fluxes). That is, the atmosphere receives a total of about 550 W/m^2 energy input from above and below, causing it to heat up and emit 217 W/m^2 of long-wave radiation upward to space and 333 W/m^2 back down to the Earth surface (Fig. 1; atmospheric radiation). That is, surface GMT and atmospheric temperatures are tightly coupled by large energy exchanges, with the surface acting as a net receiver and the atmosphere acting as a net emitter of radiation. The special role of atmospheric gasses in blocking surface radiation while themselves emitting radiation to space is revealed by the spectrum of Earth's outgoing radiation under clear sky conditions

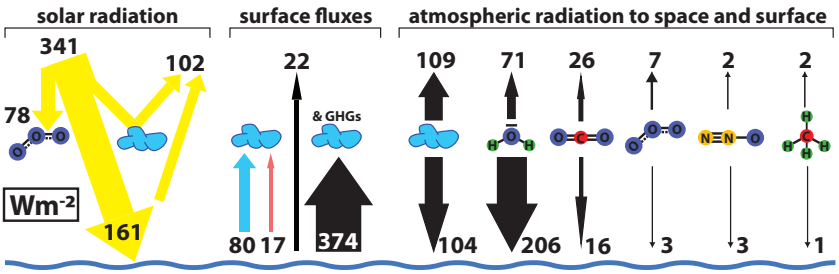

Fig. 1 Overview of energy fluxes in the climate system, separating (left) incoming solar radiation, (center) upward surface energy fluxes to the atmosphere and space, and (right) long-wave radiation from the atmosphere to space or back to the surface. Most of the total 341 W per square meter (Wm^{-2}) incoming solar radiation is absorbed by Earth's ocean and land surface, but 30% are reflected by clouds and surface and 23% are absorbed in the atmosphere by ozone (O_3), dust and smoke particles. The surface loses energy by evaporation (blue), direct conduction of heat (red) and long-wave electromagnetic radiation (black), some of which directly escapes to space but most is absorbed by clouds and greenhouse gasses (GHGs) in the atmosphere. As such the atmosphere receives on average 78 Wm^{-2} of energy from Sun and from 471 Wm^{-2} from Earth's surface, and under cloud-free conditions the GHGs emit 108 Wm^{-2} upward to space as well as 229 Wm^{-2} back down towards Earth surface (Zhong and Haigh, 2013). Ice crystals and water droplets of clouds also emit radiation upward and downward, which we estimate as 109 Wm^{-2} and 104 Wm^{-2} respectively by subtracting the clear-sky GHG energy fluxes from the atmosphere's total energy budget (Trenberth et al., 2009). The net effect of these fluxes is that the atmosphere blocks surface radiation to space and returns most of that energy back to Earth so as to maintain surface temperatures that are warmer than if Earth had no atmosphere–the greenhouse effect.

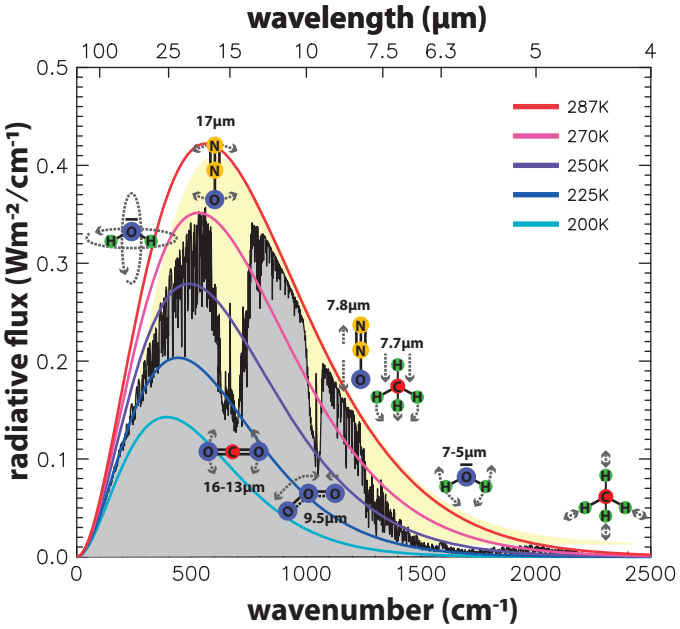

Fig. 2 The effect of greenhouse gasses (GHGs) on Earth's longwave radiation to space under clear-sky conditions (gray shaded area); where the y axis is the radiative flux per spectral wavelength shown on the top axis. The color coded curves indicate the ideal emission spectra at different temperatures, with the red curve representing the emission spectrum at typical Earth surface temperatures of 287 K (14 °C, 57 °F). That is, without GHGs Earth's radiation to space would increase by as much as the area with yellow shading. One fair description is that GHGs "take a bite" out of Earth's surface radiation to cause the greenhouse effect. The molecular motion of GHGs that cause this absorption leave a characteristic spectral fingerprint, shown schematically. The long-wave emission of Earth to space in the specific GHG spectral absorption bands originate from the GHGs, but emitted at low temperature high up in the atmosphere's tropopause and stratosphere (~225–250 K) rather than at surface temperature.

(Fig. 2), where the surface would be expected to emit a spectrum corresponding to a temperature of about 14 °C (287 K; i.e., GMT) but the actual radiation reaching space (gray shading in Fig. 2) is emitted by atmospheric constituents at relatively low atmospheric temperatures.

Because gross and net material energy exchange with space and internal sources (Q_{Earth}) are insignificant, Earth will be in radiative imbalance (positive ΔR means surplus energy input) until it is heated up and warmed enough to emit long-wave thermal radiation to space (R_{Earth})—at which point Earth reaches radiative balance ($\Delta R = 0$) and has established its stable radiative equilibrium temperature.

$$R_{solar} + Q_{Earth} - R_{Earth} = \Delta R \tag{2}$$

$$\frac{\delta GMT}{\delta t} = \frac{\Delta R}{C_P} \tag{3}$$

In this simplified formulation of Earth's energy budget the rate of warming (δGMT/δt) increases with radiative imbalance but decreases with the heat capacity (C_P) of Earth's surface environment. For example, 1 W/m^2 radiative imbalance (0.5PW) would lead to a warming rate of 0.2 K per year if we assume the heat capacity of the ~50 m ocean surface mixed layer ($C_P = 7.6 \times 10^{22}$J/K) or 0.2 K per decade if we assume the heat capacity of upper ocean (upper 500 m; $C_P = 7.6 \times 10^{23}$J/K). This is broadly consistent with the observed rate of ongoing global warming and the fact that the upper ocean has absorbed almost all of the energy from the global heating that drives the warming (Intergovernmental Panel on Climate Change, 2023).

Based on the IPCC AR6 estimated range of Earth's equilibrium climate sensitivity (ECS range from 2.5 K to 4 K of warming per 3.7 W/m^2 radiative forcing; Sherwood et al., 2020; Intergovernmental Panel on Climate Change, 2023) we should expect R_{Earth} to increase by 0.9–1.5 W/m^2 for every 1 °C of surface temperature rise. That is, starting from an initial situation with radiative balance we can estimate how much GMT needs to change (ΔGMT) to re-establish radiative balance ($\Delta R = 0$) for a given persistent radiative forcing (F). Using the roughly 17TW of fossil-fuel and nuclear primary energy use by humans as an example, the surplus energy release (F = 0.03 W/m^2) would be in radiative balance after the upper ocean was heated by 26 million PJ and GMT has warmed by about 0.034 °C-but this small change from primary energy use does not yet include the anthropogenic greenhouse effect, where a sustained doubling of atmospheric CO_2 over Holocene levels (F = 3.7 W/m^2) should lead to 2.5 K to 4 K of equilibrium climate warming.

$$\Delta GMT_F = \int_F \frac{\Delta R}{C_P}\delta t = ECS \cdot F \tag{4}$$

Because we kept our formulation simple we can integrate GMT change analytically to find that GMT asymptotically approaches its new equilibrium temperature, with an e-folding timescale (τ) that is proportional to climate sensitivity and heat capacity. That is, if we assume a 50 m deep ocean surface mixed layer as being heated, the timescale to approach radiative balance is 5 years, but if we consider the heat uptake by the entire upper ocean, the timescale may be 50 years. Even if we consider the heat capacity of the entire ocean to take up heat, the timescale is only ~400 years.

$$\Delta GMT_F(t) = \int_0^t \frac{F - ECS \cdot \Delta GMT(t)}{C_P} \delta t = ECS \cdot F \cdot \left(1 - e^{\frac{-t}{\tau}}\right) \tag{5}$$

$$\tau = ECS \cdot C_p \tag{6}$$

From this discussion we can see that temperature and climate changes on millennial or longer timescales (relevant to much of the Quaternary) reflect changes in equilibrium temperature, driven by slowly time-evolving radiative forcing (F). However, this assumption is not valid for ongoing anthropogenic global heating, because fossil-fuel use has increased much faster than the ocean's capacity to absorb the heat from the radiative imbalance caused by the anthropogenic increase in the greenhouse effect. That is, Earth is currently heating up fast because of a large radiative imbalance.

Greenhouse gasses and climate sensitivity

Dry air is a gas mixture composed of 78% dinitrogen (N_2), 21% dioxygen (O_2), 1% argon (Ar) and other trace gasses, giving a total of 1.38×10^{20} mol of N_2, 0.37×10^{20} mol of O_2, 0.02×10^{20} mol of Ar, and total mass of 5.15×10^{18} kg. These gasses are well mixed in the atmosphere yielding constant mixing ratios in space. It takes about 20 Joules (J) of energy to heat up 1 mol of ideal diatomic gas at constant pressure by one degree Kelvin, the isochoric heat capacity (c_p), with ⅖ of that energy accelerating random molecular movement in three-dimensional space and another ⅖ accelerating two degrees of rotation of these molecules. That is, to heat Earth's entire atmosphere by one degree Kelvin requires about 3.5×10^{21} Joules, corresponding to less than 5% of the total heat capacity of the 50 m surface layer of the ocean.

$$\left(\frac{\delta E}{\delta T}\right)_p = C_p = c_p \cdot N_{atm} = \frac{5}{2} R \cdot N_{atm} = 20 \frac{J}{mol \cdot K} \cdot 1.773 \times 10^{20} mol = 3.5 \times 10^{21} \frac{J}{K} \tag{7}$$

Water vapor (H_2O) in the atmosphere plays a special role in Earth's climate: first because it can change phase between vapor, liquid and ice, and second because the two hydrogen atoms are prone to vibrate about the central oxygen atom, unlike diatomic gasses. The total rate of surface evaporation is about 500,000 cubic kilometers of water per year (Trenberth et al., 2009) corresponding to about 4×10^{16} W (80 W/m^2) of surface thermal energy being converted to latent heat contained in the water vapor that is released to the atmosphere–a very large flux compared to the heat capacity of the atmosphere. This is because air can hold about 2% H_2O at surface temperature and pressure before condensation occurs, which converts the latent heat of water vapor back to thermal energy in the atmosphere. The net effect of this hydrologic cycle is to cool the surface by heating the atmosphere where it rains and snows, but there is no net change in the total amount of energy in the climate system. At any one moment the atmosphere only holds about 13,000 cubic kilometers of water in vapor form (7×10^{17} mol of water molecules, average concentration 0.4%), but because of the large latent heat of vaporization (40.8 kJ/mol) the atmosphere's 2.8×10^{22} Joules of water vapor latent heat content and transport are critical components of Earth's weather and climate. All else being equal, higher temperatures increase the amount of water in the atmosphere.

The second aspect of H_2O that sets it apart from the main diatomic gasses of the atmosphere relates to the low energy needed to make H_2O molecules rotate and vibrate, which moves the two positively charged protons relative to the negatively charged electrons orbiting the central oxygen atom. As a principle of quantum mechanics each of these vibrational modes can store energy only in multiples of one specific quanta of energy (ΔE), corresponding to the resonant frequency of that mode. While the direct effect of these vibrational modes on the heat capacity of air are small, they can spontaneously emit and absorb photons of electromagnetic radiation corresponding to their specific vibration energy quanta (Eq. 8, where c is the speed of light and h is Planck's constant). In the case of H_2O, the highest-energy vibrational modes absorb some incoming long-wave solar radiation–corresponding to wavelengths ($\lambda_{\Delta E}$) in the range 0.7–3 μm that would not otherwise vibrate at atmospheric temperature-whereas the lower-energy rotations and vibrations can effectively absorb all wavelengths of thermal radiation emitted by Earth's surface (4–50 μm) except for radiation in the wavelength range 8–12 μm (Fig. 2). This wave band is often referred to as the "atmospheric window" in the Earth's greenhouse effect because it lets heat escape. That is, while the amount of rotational and vibrational energy stored in water molecules is dwarfed by the thermal and latent heat of the atmosphere, it is primarily the emission of long-wave radiation by atmospheric water molecules and clouds to space that balances Earth's radiative budget vis-a-vis absorbed solar radiation (Fig. 1).

$$\Delta E = \frac{hc}{\lambda_{\Delta E}} \Leftrightarrow \frac{hc}{\Delta E} = \lambda_{\Delta E} \tag{8}$$

Other trace gasses in air during the preindustrial Holocene period were relatively stable at 280 parts-per-million (ppm; with 1000 ppm equal to 0.1%) of carbon dioxide (CO_2), 800 parts-per-billion (ppb; where 1 ppb is 0.0001%) of methane (CH_4), 300 ppb of ozone (O_3) concentrated in the stratosphere, and 270 ppb of nitrous oxide (N_2O). Of these gasses CO_2, CH_4 and N_2O

now rise rapidly due to human-caused emissions while O_3 declined in the stratosphere as a consequence of chlorofluorocarbon (CFC) refrigerant release. Just like H_2O these gasses have a central atom to vibrate about without stretching the bond-length between the atoms, and so they can store energy in additional vibrational modes that can get excited by molecule collisions at atmospheric temperature. For that reason, the isochoric heat capacity of these gasses is greater than that of diatomic gasses, again with an insignificant effect on the atmosphere's total heat capacity because of the low concentration of these molecules (<0.5%). However, and more relevant, these additional vibration modes also absorb and emit photons in the long-wave spectrum, partly overlapping with absorption and emission of H_2O. That is, at some wavelengths CO_2, N_2O and CH_4 can directly exchange photons of energy with H_2O but in the range 8–12 μm range where H_2O cannot emit or absorb it is primarily the trace gasses that absorb thermal radiation from the surface and themselves emit thermal radiation to space (Figs. 1 and 2; Zhong and Haigh, 2013). This latter radiative effect (ΔR) can be estimated with spectrally resolved radiative balance models and expressed as simplified functions of the change in the respective trace gas concentration (Etminan et al., 2016; omitting interaction terms between CO_2, CH_4 and N_2O):

$$\Delta R_{CO2} \approx 5.36 \frac{W}{m^2} \cdot ln\left(\frac{CO_2^{new}}{CO_2^{initial}}\right) \tag{9a}$$

$$\Delta R_{CH4} \approx 0.043 \frac{W}{m^2} \cdot \left(\sqrt{CH_4^{new}} - \sqrt{CH_4^{initial}}\right) / \sqrt{ppb} \tag{9b}$$

$$\Delta R_{N2O} \approx 0.117 \frac{W}{m^2} \cdot \left(\sqrt{N_2O^{new}} - \sqrt{N_2O^{initial}}\right) / \sqrt{ppb} \tag{9c}$$

$$\Delta R_{GHG} \approx \Delta R_{CO2} + \Delta R_{CH4} + \Delta R_{N2O} \tag{9d}$$

Increases in CO_2, CH_4 and N_2O all lead to a net positive radiative effect that acts to heat up Earth by blocking outgoing radiation, and for this reason these gasses are referred to as greenhouse gasses (GHG). That is, like the glass in a greenhouse these gasses transmit the incoming sunlight but impede the escape of heat to cause the greenhouse effect, a warming "blanket" keeping the inside above the temperature of the surrounding environment. Water vapor is also counted as a greenhouse gas, indeed accounting for most of Earth's natural greenhouse effect (Fig. 1). However, the water holding capacity of air depends strongly on temperature and atmospheric water concentration therefore cannot change independently from climate. For that reason the water vapor response to 1 K warming will cause about 1.15 W/m^2 positive climate forcing that amplifies the initial warming, which is referred to as a positive (amplifying) feedback (λ_{H2O}); where the symbol lambda is conventionally used to refer both to feedback parameters in the units of W/m^2/K and to electromagnetic wavelength (Eq. 8). Likewise, for each 1 K of warming Earth's total emissions of long-wave radiation to space increase by about 3.2 W/m^2 according to Planck's Law (λ_{Planck}), a negative radiative climate forcing that acts to restore Earth's radiative balance with space (see Eq. 2). Taken together Planck and water vapor feedbacks suggest that Earth needs to heat up by 1 K for every 2 W/m^2 radiative forcing in order to establish radiative balance with space, but there are other significant feedbacks that need to be accounted for (Sherwood et al., 2020). These include additional positive feedbacks from (1) sea ice, snow cover and vegetation changes that reduce Earth's effective surface albedo with warming (α in Eq. 1b; $\lambda_{surface}$), and from (2) various net-positive cloud feedbacks (λ_{clouds}, λ_{other}) that increase the sensitivity of Earth's equilibrium temperature to radiative forcing at a negative net equilibrium climate feedback. Currently available evidence from theory, models, historical observations and paleoclimate studies suggests (λ_{ECS}) is likely between −0.95 W/m^2/K and −1.4 W/m^2/K (Sherwood et al., 2020).

$$\lambda_{ECS} = \lambda_{Plank} + \lambda_{H2O} + \lambda_{surface} + \lambda_{clouds} + \lambda_{other} \tag{10}$$

$$\Delta GMT_{ECS} = ECS \cdot \Delta R_{GHG} = \frac{-\Delta R_{GHG}}{\lambda_{ECS}} \tag{11}$$

Using anthropogenic greenhouse gas forcing as an example, as of today the direct anthropogenic GHG radiative forcing of higher CO_2, CH_4 and N_2O is about 2.5 W/m^2 (R_{GHG}), Earth surface and atmosphere have already warmed by about 1 K to increase Earth's long-wave emissions to space by likely more than 1 W/m^2 (λ_{ECS}). This leaves a residual ~1 W/m^2 radiative imbalance observed by satellites, which continuously heats the much larger heat capacity of the upper ocean. That is, if we stabilize greenhouse gasses now the climate system will continue to heat up by maybe another 1 K before the Earth would be again in radiative balance with space. If we go further and include slow-acting positive feedbacks from the increase in albedo with atmospheric dustiness (λ_{dust}) and from ice sheet extent (λ_{ice}) we arrive at the Earth System Sensitivity (ESS, λ_{ESS}) of ~2 K of warming per 1 W/m^2 of radiative forcing, relevant to natural climate changes over the Quaternary period (Fig. 3).

$$\lambda_{ESS} \approx \lambda_{ECS} + \lambda_{dust} + \lambda_{ice} \tag{12}$$

$$\Delta GMT_{ESS} = ESS \cdot \Delta R_{GHG} = \frac{-\Delta R_{GHG}}{\lambda_{ECS} + \lambda_{dust} + \lambda_{ice}} \tag{13}$$

The key consequence of this derivation is that even modest changes in the trace concentration of greenhouse gasses can have a significant effect on global temperature levels, especially when allowing millennia for the positive feedbacks to unfold. The radiative forcing from CO_2 change (R_{CO2}) dominates anthropogenic climate change, and it appears to have been an important driver of Quaternary climate change.

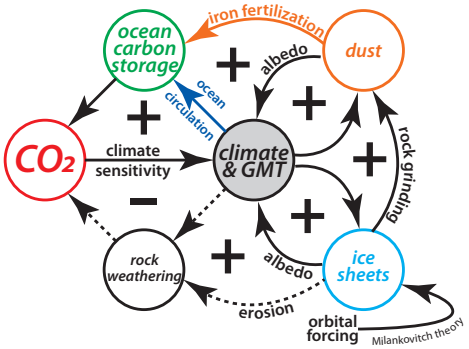

Fig. 3 Key feedback dynamics relevant to the regulation of Quaternary climate. Soon after the discovery of ice ages it was hypothesized that variations in Earth's orbit about the Sun were responsible for repeated ice age cycles, a theory formalized by Milutin Milankovitch and colleagues some 100 years ago. In that view, insolation in the subpolar boreal zone (65°N) is critical for the development of northern ice sheets, which increase planetary albedo, lower global mean temperatures (GMT) to encourage further ice sheet growth in a positive (+) ice albedo feedback. With the discovery of ice age cycles in atmospheric CO_2 we began to realize that greenhouse gas radiative forcing and Earth's climate sensitivity are critical components of Earth's climate system. For example, dust in the atmosphere increases with cold and dry glacial climate conditions as well with ice sheet grinding of bedrock, and that dust increases Earth's albedo to exacerbate cooling. Further, iron-bearing dust fertilizes phytoplankton in the ocean to increase ocean carbon storage and lower CO_2, which further cools climate through a positive climate/carbon cycle feedback. Ocean circulation appears to be another critical component in governing ocean carbon storage and atmospheric CO_2 radiative forcing of climate in a positive feedback, in contrast to land carbon storage and the direct sea level effect of ice sheets that yield negative feedbacks (not shown). This raises the possibility that orbital forcing directly affected climate and/or ocean circulation to yield climate change driven by ocean storage of CO_2 rather than the ice sheets' albedo effect, in contrast to Milankovitch theory. It remains an open research question how orbital forcing translated into Quaternary climate change. Likewise, the role of rock weathering in driving Quaternary climate remains uncertain, because weathering is expected to slow with glacial cooling and but increase with glaciation, yielding negative (–) and positive (+) feedbacks that support the view that long-term tectonic trends caused the bipolar glaciations that define the Quaternary by changing atmospheric CO_2.

Climate-carbon cycle feedbacks

So far we have discussed the effects of greenhouse gas concentrations on Earth's climate and temperature, but we have not considered if and why greenhouse gasses would vary in response to climate change (Fig. 3). These are critical questions for our understanding of the Earth's natural long-term climate-carbon cycle coupling and below we outline six climate feedbacks that can affect atmospheric CO_2 concentration and radiative forcing (Eqs. 14a–14g):

1. CO_2 is more soluble in seawater at lower temperature such that a colder ocean can absorb CO_2 from the atmosphere, with about 4% of CO_2 increase per degree warming (ΔT).
2. When ice sheets melt the mass of seawater increases and its salinity decreases so that the ocean can store more carbon, causing about 7% reduction in atmospheric CO_2 per 100 m of sea-level rise (ΔSL).
3. Carbon storage in forests and soils on land removes carbon from the atmosphere and ocean, with about 1% of CO_2 reduction per 100PgC of land carbon uptake (ΔC_{Land}).
4. A strengthening in the ocean's biological carbon pump can remove carbon from the atmosphere, with about 6% CO_2 reduction per 100PgC of additional deep ocean respired carbon storage ($\Delta C_{BP\text{-}OM}$).
5. A strengthening in the ocean's biological $CaCO_3$ pump stores more carbon in the deep ocean but acidifies the upper ocean to cause higher atmospheric CO_2, with about 6% CO_2 increase per 100PgC of additional deep ocean storage of carbon regenerated by $CaCO_3$ dissolution ($\Delta C_{BP\text{-}CaCO3}$).
6. Any increase in weathering or decrease in pelagic calcification by open ocean plankton results in a alkalinity supply surplus that raises ocean $CaCO_3$ saturation state, increases the water-depth of the calcite saturation horizon (CSH) and thereby resolves the initial alkalinity imbalance, with about 1.4% CO_2 decrease per 100 m of steady-state CSH deepening (ΔCSH).

These estimates include the projected secondary feedbacks from ocean carbonate compensation that take about 10,000 years to fully unfold and are thus relevant to slow modes of Quaternary climate change (Hain and Sigman, 2024). Because all of these feedbacks cause fractional CO_2 change their radiative effects are independent and can simply be added up (Eq. 14a), where a 1% CO_2 increase corresponds to about 0.05 W/m^2 of radiative forcing.

$$\Delta R_{CO2} \approx \Delta R^{T}_{CO2} + \Delta R^{SL}_{CO2} + \Delta R^{LandC}_{CO2} + \Delta R^{BP\text{–}OM}_{CO2} + \Delta R^{BP\text{–}CaCO3}_{CO2} + \Delta R^{CSH}_{CO2} \quad (14a)$$

$$\Delta R_{CO2}^{T} = \frac{4\%}{K} \cdot \frac{0.05W/m^2}{1\%} \cdot \Delta T \tag{14b}$$

$$\Delta R_{CO2}^{SL} = \frac{-7\%}{100m} \cdot \frac{0.05W/m^2}{1\%} \cdot \Delta SL \tag{14c}$$

$$\Delta R_{CO2}^{LandC} = \frac{-1\%}{100PgC} \cdot \frac{0.05W/m^2}{1\%} \cdot \Delta C_{land} \tag{14d}$$

$$\Delta R_{CO2}^{BP-OM} = \frac{-6\%}{100PgC} \cdot \frac{0.05W/m^2}{1\%} \cdot \Delta C_{BP-OM} \tag{14e}$$

$$\Delta R_{CO2}^{BP-CaCO3} = \frac{+6\%}{100PgC} \cdot \frac{0.05W/m^2}{1\%} \cdot \Delta C_{BP-CaCO3} \tag{14f}$$

$$\Delta R_{CO2}^{CSH} = \frac{-1.4\%}{100m} \cdot \frac{0.05W/m^2}{1\%} \cdot \Delta CSH \tag{14g}$$

Some of these feedbacks are relatively closely tied to climate change. For example, ocean temperature and sea level change are effectively controlled by Earth's radiative balance and the hydrologic mass balance of polar ice sheets. Likewise, changing surface temperature and hydro-climate can cause expansion or contraction of forest biomes and affect the rate of plant and soil organic carbon turnover, which would drive a change in total land carbon storage (ΔC_{Land}). In contrast, changes in ocean carbon storage by the ocean's biological pump (ΔC_{BP}) depend on changes in the physical conditions and circulation of the ocean, chemical inputs of trace nutrients to the polar ocean surface, as well as the dynamic ecosystem responses to these changes. That is, the response of the biological pump to climate–past or future–is not straightforward and remains a critical target for paleoceanographic reconstructions (Sigman et al., 2021) and process-based Earth System Modeling (Gottschalk et al., 2019). Similarly, changes in the ocean's overall $CaCO_3$ saturation state depend on the impact climate has on continental weathering as well as the biological response of biologically-controlled $CaCO_3$ production to physical, chemical and biological ocean changes–an area relevant to anthropogenic ocean acidification research and potential pathways for mitigating anthropogenic climate change (Intergovernmental Panel on Climate Change, 2023).

Finally, there is another climate-carbon cycle feedback relevant to the Quaternary period, Earth has a negative feedback that restores the balance between geologic CO_2 sources (mainly volcanic CO_2 emissions and weathering of organic carbon-rich rock formations) and CO_2 sinks (mainly the weathering of silicate minerals). Because the rate of silicate weathering on land increases with temperature and net precipitation the Earth System will tend towards the particular atmospheric CO_2 level that yields the climate conditions that allow silicate weathering to match the geologic carbon sources. Hence, silicate weathering acts as a thermostat setting atmospheric CO_2 and climate based on geologic forcing (Walker et al., 1981), and thus it has several quasi-stable settings which are related to tectonic processes (e.g. seafloor spreading, continental drift and mountain building) or climate related changes in weathering rate or intensity (e.g., glacial erosion; Fig. 3). However, because of the relatively slow rates of these geologic fluxes relative to the large carbon inventory of the climate system the negative silicate weathering feedback operates only on a million year timescale, too slow to cause more than gradual secular trend in atmospheric CO_2 over the Quaternary period.

Greenhouse-gas reconstructions

There are three ways to estimate past greenhouse gas concentrations (GHGs) and their radiative climate forcing (R_{GHG}): (1) we can empirically reconstruct GHGs using direct and indirect approaches, (2) we can use carbon cycle models to project reconstructed empirical climate and carbon cycle reconstructions, and (3) we can use process-based coupled climate-carbon cycle models (Earth System Models) to predict CO_2 ab initio. Comparing the results of these three approaches helps characterize the uncertainties and biases in empirical reconstructions, facilitates attribution of GHG change to climate-carbon cycle feedbacks, and challenges our understanding of the Earth System as a whole.

Empirical reconstructions of GHGs can be obtained either directly from air-bubbles preserved in polar ice sheets or indirectly from some other sample material that faithfully records a chemical or isotopic signal related to changing GHGs. Unfortunately there are no "proxy" archives currently known that could be used to indirectly reconstruct atmospheric CH_4 and N_2O concentrations, but a number of proxy systems have been developed to reconstruct atmospheric CO_2. These indirect CO_2 proxies include the density of leaf pores, or stomata in preserved terrestrial plants, boron isotope composition of planktonic foraminifera, and the carbon isotope composition of alkenones and other organic compounds extracted from marine sediment cores and of pedogenic (soil) carbonates. Other indirect CO_2 proxies have not been widely used for the Quaternary period, but they offer invaluable information through the larger changes through deep geologic time.

Comparing direct and proxy GHG reconstructions with model simulations fundamentally requires independent and accurate age information (Yun et al., 2023), which is always a challenge for the indirect proxies based on sedimentary archives. Moreover, each approach to reconstruct GHGs at any given age may have its own specific biases and uncertainties, which are especially difficult to estimate for indirect proxy reconstructions and numerical models. One thing that is clear is that ocean carbon chemistry and cycling effectively control atmospheric CO_2 on timescales from thousands to millions of years relevant to the Quaternary period.

That is, the Quaternary is too short to allow for significant changes in the total carbon inventory of the climate system but climate-carbon cycle feedbacks may have changed the partitioning of that carbon inventory between the ocean, atmosphere, and land surface–a key theoretical mass balance constraint arising from carbon cycle modeling.

Ice core GHG reconstructions

The idea that air bubbles trapped in ice may directly record atmospheric GHG concentrations originated in the 1960s, at the same time as direct air CO_2 measurements first demonstrated that anthropogenic carbon emissions were accumulating as CO_2 in the atmosphere. However, early attempts by Swiss and French scientists to reconstruct CO_2 from gas bubbles trapped in alpine glaciers failed because these small bodies of ice collect too much extraneous mineral rock debris and reactive organic matter to preserve the reactive composition of enclosed air bubbles. This led glaciologists to venture first to the summit of the Greenland ice sheet and then to various places deep in the Antarctic interior in search of long, clean and continuous ice core samples to accurately reconstruct atmospheric GHGs back through time–what would become one of the most significant successes in (paleo)climate science. Particular recognition for that advance is due to the Greenland Ice Sheet Project (GISP, 1970s) led by Swiss, Danish and American scientists, the Vostok station ice core drilling project led by Soviet/Russian and French scientists (1970s–90s), the European Greenland Ice Core Project (GRIP, 1990s), and the European Project for Ice Coring in Antarctica (EPICA, 1990s–2000s). From this body of work we now have a detailed, replicated and accurately dated record of atmospheric CO_2, CH_4 and N_2O for the last 800 thousand years (Fig. 4). The ongoing "Beyond EPICA" project (2020s) is seeking to extend the continuous ice core record of GHGs to 1.5 million years or longer.

Beyond the 800 kyrs reach of the continuous ice core GHG records, older snapshots of ice with trapped air have been found preserved in the Antarctic interior. These "blue ice" areas are stratigraphically disturbed from the continual flow of the ice cap, but bring the advantage of being able to find older ice much closer to the surface. In the Allan Hills, in Antarctica CO_2 measurements

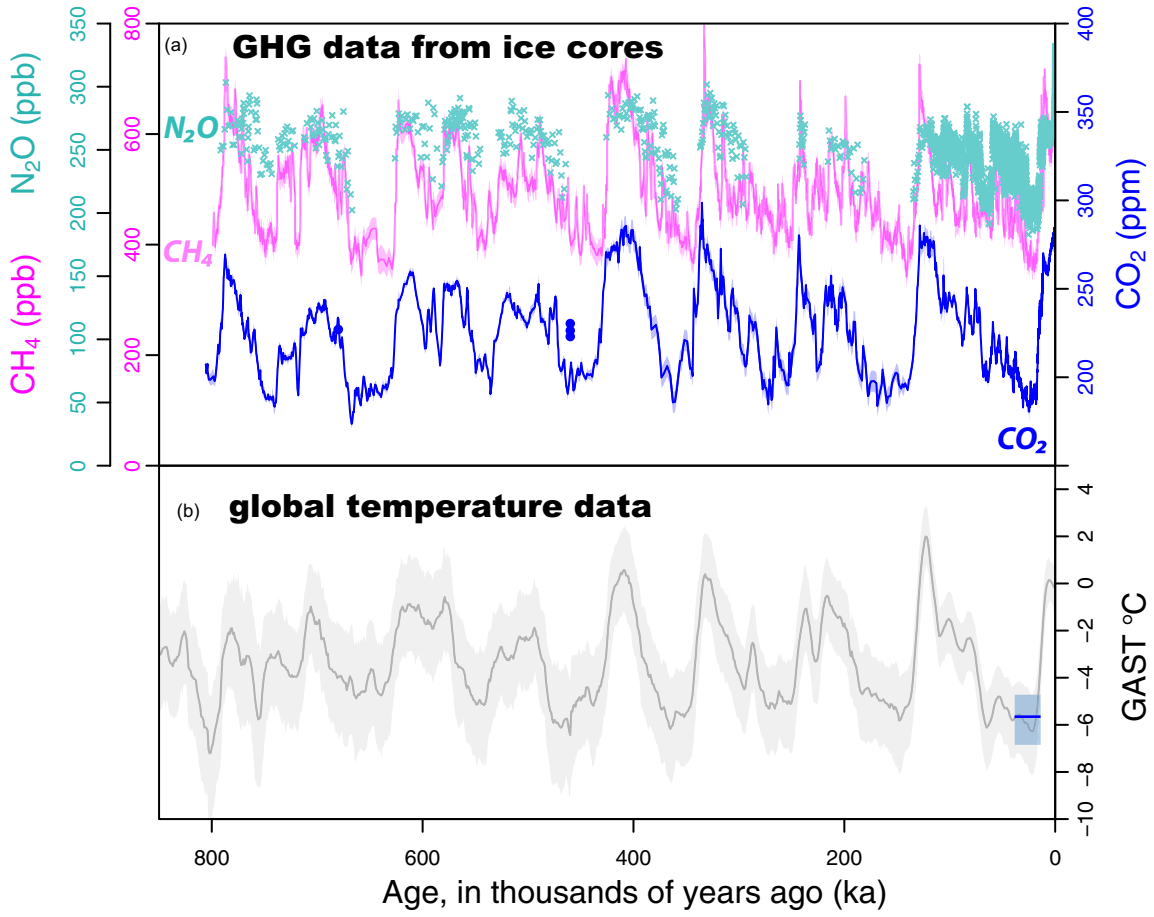

Fig. 4 Greenhouse gasses and global temperature over the last 800 kyrs. (a) Records of past atmospheric gas composition from bubbles of ancient atmosphere trapped within antarctic ice cores. CO_2 (in parts per million, right axis) is shown in blue (Bereiter et al., 2015), including discrete samples of disturbed ice in blue points (Yan et al., 2019). CH_4 (in parts per billion, first left axis) is shown in pink (Loulergue et al., 2008). N_2O (in parks per billion, second left axis) is shown in teal points (Schilt et al., 2010). (b) An estimate of global average surface temperature (GAST, in degrees Celsius from the preindustrial, Snyder, 2016) from mixed terrestrial and marine proxy records.

have been obtained from as old as 1.9 million years, more than twice the age of the oldest continuous ice core, and even examples of chemically disturbed pre-Quaternary ice have been identified (Yan et al., 2019). Dating can be performed indirectly by the analysis of meteorites within the ice, or directly via the ^{40}Ar atmosphere geochronometer, which arises from the decay of crustal ^{40}K to ^{40}Ar over time. The drawbacks of this method are that it is not precise enough to recover relative ages of the ice within a sample set, and it is near impossible to fully know the proportion of glacial versus interglacial intervals recovered by a suite of samples. However, most of the advantages of direct measurement of air trapped in clean ice remain, including the other measurements of the other trace GHGs CH_4 and N_2O as well as other climate proxies.

Boron isotope CO_2 proxy

The 5th element of the periodic table, boron, is a minor component of seawater (~4 ppm), where it has a long residence time, and in the Quaternary can be considered more or less fixed in concentration. In sea water boron is found in two primary compounds: boric acid ($B(OH)_3$) and borate ion ($B(OH)_4^-$) which undergo the following equilibrium reaction:

$$B(OH)_3 + H_2O \Leftrightarrow B(OH)_4^- + H^+ \tag{15a}$$

$$pH = -\log H^+ = pK_B + \log \frac{B(OH)_4^-}{B(OH)_3} \tag{15b}$$

This equilibrium is pH dependent, as marked by the presence of free protons, H^+ ions. At pH ~8.2, the pH of our modern oceans, boric acid makes up ~75% of the oceanic boron, and borate ion ~25%, and any increase in pH will be accompanied by the conversion of boric acid to borate ion; and vice versa for a pH decrease.

Boron also has two stable isotopes, ^{10}B (~20%) and ^{11}B (~80%) and these fractionate in the above borate/boric acid equilibrium reaction so that the boric acid is enriched in ^{11}B and the borate ion enriched in ^{10}B (heavier isotopes have an affinity for molecules with stronger bonds). The fractionation factor α_B corresponds to the ratio of the boric acid and the borate isotope ratios (Eqs. 16a and 16b), which differ by about 2.72% corresponding to an isotope effect ε of 27.2 ‰. Thus, when the relative proportion of borate/boric acid varies (i.e., pH change), so must the isotope ratios of the two boron species (Eq. 16c).

$$\alpha_B = \frac{^{11}B(OH)_3/^{10}B(OH)_3}{^{11}B(OH)_4^-/^{10}B(OH)_4^-} = \frac{^{11/10}R_{B(OH)_3}}{^{11/10}R_{B(OH)_4^-}} = 1.0272 = 1 + \varepsilon \tag{16a}$$

$$\delta^{11}B = \frac{^{11/10}R_{sample}}{^{11/10}R_{reference}} - 1 \Leftrightarrow \delta^{11}B_{B(OH)_4^-} \simeq \delta^{11}B_{B(OH)_3} + \varepsilon \tag{16b}$$

$$\delta^{11}B_t \cdot \left(B(OH)_3 + B(OH)_4^-\right) = \left(\delta^{11}B_{B(OH)_4^-}\right) \cdot B(OH)_4^- + \left(\delta^{11}B_{B(OH)_4^-} - \varepsilon\right) \cdot B(OH)_3 \tag{16c}$$

Borate ions are charged and tetragonal in shape, which is similar to the carbonate ion (CO_3^{2-}) that forms the structure of marine calcifiers (corals, crustaceans, and plankton groups). Thus the $\delta^{11}B$ of borate from water of a particular pH is preserved inside the shells of these fauna and flora. One group in particular, the planktic foraminifera, provide an excellent record of $\delta^{11}B$ of borate in ancient sea water, and that is because they are widespread, well preserved in cored marine sediments, and easy to identify. The $\delta^{11}B$ of borate in foraminifera shells indicates the pH of the ocean water as reflected in the microenvironment around the individual foraminifer (Rae, 2018; Hönisch et al., 2023):

$$pH = pK_B - \log\left(\frac{\delta^{11}B_{SW} - \delta^{11}B_{B(OH)_4^-}}{\delta^{11}B_{SW} - \alpha \cdot \delta^{11}B_{B(OH)_4^-} - \varepsilon}\right) \tag{16d}$$

The unique power of the boron isotope pH proxy system for the reconstruction of atmospheric CO_2 comes from its intimate link to the seawater carbonate chemistry, effectively determining how much of the dissolved inorganic carbon (DIC) of the seawater is in the form of aqueous CO_2 that can exchange with the atmosphere ($H_2CO_3^*$ in Eq. 17a). Critically, any reconstructed change in pH (ΔpH) reflects an exponential change in aqueous CO_2 (i.e., a proportional change in $\Delta \ln CO_2$) if the timescale of the change is short enough to limit significant changes in the ocean total carbon inventory (i.e., $\Delta \log HCO_3^-$ is close to zero; Eq. 17b), which is appropriate for Quaternary climate-carbon cycle variability and transitions, but not for longer (Myr) timescales. As such, when combined with Eq. (9a), reconstructions of pH change (ΔpH) can directly yield precise estimates for past CO_2 radiative climate forcing (R_{CO2} in Eq. 17c; compare to Fig. 5d) and for the expected global mean temperature change (ΔGMT in Eq. 17d) on short to medium time scales. Notably, the boron isotope proxy system offers robust constraints on ΔpH and $\Delta \log CO_2$, which need to be further calibrated to yield absolute pH and CO_2 (Hain et al., 2018).

$$pH = pK_2 + \log \frac{CO_3^{2-}}{HCO_3^-} = pK_1 + \log \frac{HCO_3^-}{H_2CO_3^*} = pK_W + \log OH^- \tag{17a}$$

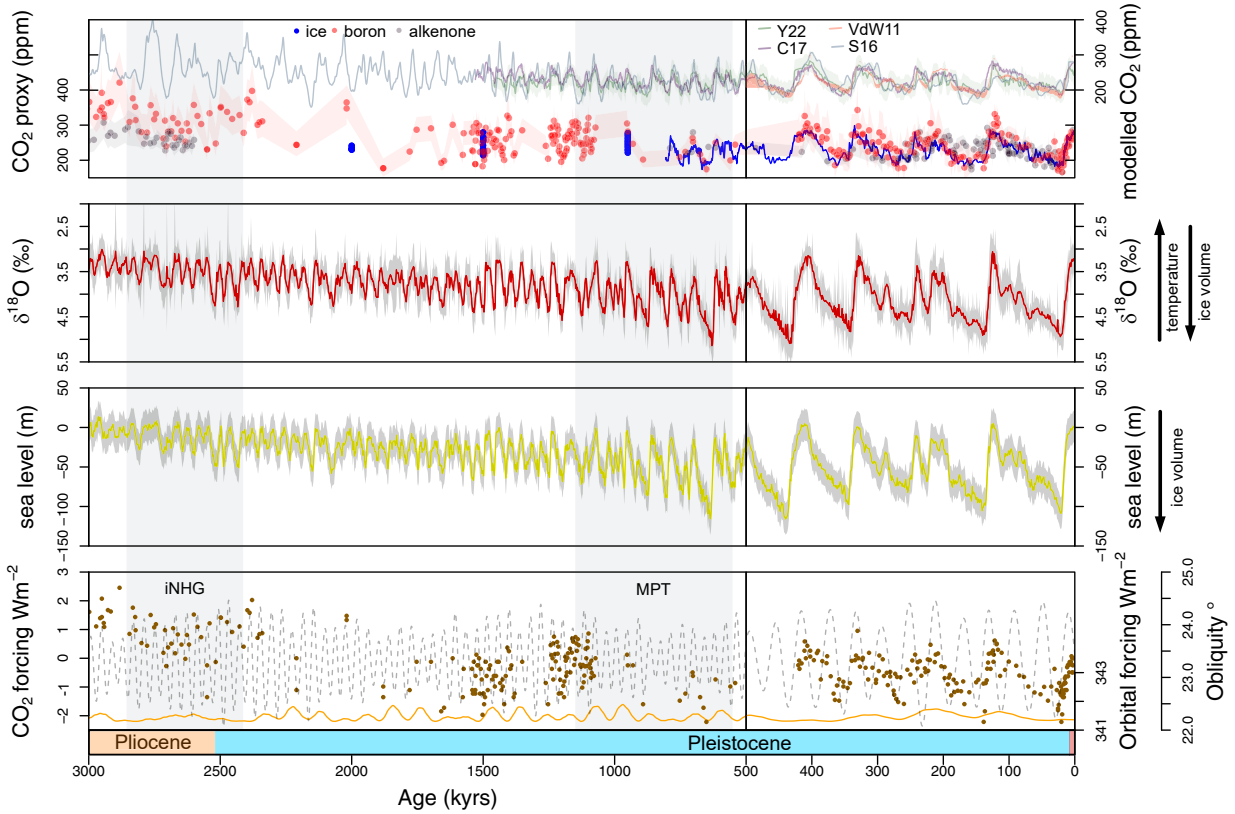

Fig. 5 CO_2 records and climate events over the Quaternary. (a) CO_2 proxy data from ice cores (blue), boron isotopes in planktic foraminifera (red) and alkenones (gray), all plotted against left side axis. Model or proxy driven CO_2 data from δ^{13}FA (Yamamoto et al., 2022), a carbon cycle box model (C17, Chalk et al., 2017), and models of intermediate complexity (VdW11, Van De Wal et al., 2011; S16, Stap et al., 2016), plotted against right side axis (200 ppm positive offset from proxy data). (b) $\delta^{18}O$ (oxygen isotope ratio) stack of deep ocean sites from benthic foraminifera, commonly used as a proxy for climate state as their composition represents a combination of temperature and global ice volume. (c) sea level proxy data showing glacial lowstands and interglacial highstands. (d) Orbital and GHG forcing, total incoming radiative forcing from orbit (watts per meter squared, orange right axis), largely controlled by eccentricity is ~5× smaller than the radiative forcing exerted by CO_2, which is a climate driver and feedback, shown in brown points (watts per meter squared, left axis). Obliquity (in degrees from perpendicular to the solar plane) is shown on the second left axis. Note the split x-axis scaling at 500 kyrs.

$$\Delta pH = \Delta \log HCO_3^{2-} - 2.3 \cdot \Delta \ln CO_2 + \Delta pK_0 + \Delta pK_1 \approx -2.3 \cdot \Delta \ln CO_2 \tag{17b}$$

$$\Delta R_{CO2} \approx -12.34 \frac{W}{m^2} \cdot \Delta pH \tag{17c}$$

$$\Delta GMT_{ESS} \approx ESS \cdot \Delta R = \frac{12.34 \frac{W}{m^2} \cdot \Delta pH}{\lambda_{ECS} + \lambda_{dust} + \lambda_{ice}} \tag{17d}$$

One important test case for the boron isotope proxy system is the direct comparison to atmospheric CO_2 from ice cores (Section "Ice core GHG reconstructions"). In this comparison boron isotope derived pH estimates correspond to logCO_2 changes with a slope that is near the theoretical prediction from changes driven by changing DIC (Fig. 5d; Hain et al., 2018; De La Vega et al., 2023). This direct comparison provides confidence in the use of boron isotopes during the Quaternary as the theoretical relationship is shown to be upheld by empirical data over the last 800 kyrs. Records of boron isotope based CO_2 cover the entire Quaternary but at different temporal resolution for the specific intervals are discussed in section "Carbon dioxide as a driver of Quaternary climate".

Alkenone based proxies

The isotopic fractionation of carbon between dissolved inorganic carbon (DIC) and the long chain biomass of alkenone producers is controlled by the CO_2 concentration. In brief, as CO_2 diffuses through the phytoplankton cell membrane the concentration of CO_2 inside the cell is proportional to the available aqueous CO_2 in seawater. The carbon fixing enzyme RuBisCO preferentially uptakes ^{12}C when compared to ^{13}C (or ^{14}C), and as CO_2 in the water and cell increase, this preference for the lighter isotope becomes stronger and will be preserved in the organic alkenone molecules produced by haptophyte algae phytoplankton.

$$\varepsilon_p^{sample} = \varepsilon_f^{reference} - \frac{b}{CO_2} \tag{18a}$$

$$CO_2 = \frac{b}{\varepsilon_f^{reference} - \varepsilon_p^{sample}} \tag{18b}$$

However, this process is complicated by many factors, such as active transport of CO_2 at low concentrations, phytoplankton growth rate and cell size; these can be termed "b" as in the equation above. The active transport (or carbon concentration mechanism, CCM) in particular makes the interpretation of alkenone CO_2 proxy data during the Quaternary difficult (Zhang et al., 2019), as CO_2 is thought to have remained below modern, and largely below pre-industrial levels throughout the period. However, alkenone records are relatively easy to generate, and in the right sites and with the right auxiliary data provide a useful constraint on past CO_2.

Other archives

Pedogenic carbonates

Carbonate deposits in soil normally originate from dissolved CO_2 in the soil/ground water. In arid environments this CO_2 concentration is likely to be in near equilibrium with the atmosphere, at least where respiration from plant roots and fauna are minimal. However, estimates of the depth of precipitation, temperature, and respiration levels are required as well as the $\delta^{13}C$ of CO_2 in the atmosphere. Some other problems arise aside from the usual problems of dating in terrestrial deposits, that is that the formation of these carbonates may take many hundreds or thousands of years, smoothing out climate signals. Thus they are largely unsuited to the creation of high resolution or orbitally resolved Quaternary records.

Stomatal density

Despite the importance placed on CO_2 in regulating climate, its low overall concentration in the atmosphere renders it difficult to be utilized by terrestrial plant life. CO_2 is able to enter a plant's leaves through holes or pores called stomata. During photosynthesis, plants convert CO_2 into oxygen and carbohydrates, using water or other electron donors and energy, which for photosynthesis originates from collected sunlight.

$$CO_2 + H_2O + energy \Rightarrow CH_2O + O_2 \tag{19}$$

To increase the availability of CO_2 for this reaction, plants increase the density of stomata they have in relation to the partial pressure of CO_2 in the atmosphere. However, given that increasing the stomata to leaf surface area ratio also increases the rates of water loss by transpiration from the leaf, water availability/stress are also important factors to consider. The drought effect can be accounted for by applying a species-specific stomatal index (SI), which typically uses the epidermal cell density to account for drought stress.

In general stomata proxies are hampered in the geological record by the requirement for samples of a known age and species/genus which are well enough preserved to provide reliable stomata counts. There are also requirements for some knowledge of water stress and sample altitude which further limits their applicability.

Land plant derived carbon isotopes

Alongside stomatal frequencies another plant based CO_2 proxy is the quantification of leaf gas exchange, which can be estimated by the fossilized $\delta^{13}C$ of C3 plants. As all plants preferentially uptake the light carbon isotope ^{12}C relative to the heavier ^{13}C, the ratio of these isotopes in comparison to their ratio in the background atmosphere can be related to the concentration of CO_2 gas in the atmosphere. This relationship is also dependent on a number of other parameters, including: mean annual precipitation, plant functional type, and the $\delta^{13}C$ of the atmosphere. Given the many uncertainties we do not include these proxy types further with the exception of one record.

In theory, the $\delta^{13}C$ of fatty acids in land plant ecosystems can respond to atmospheric CO_2 via the competition between C3 and C4 plants. Briefly, C4 plants are better suited to low CO_2 environments and show less fractionation in their carbon isotopes relative to their C3 counterparts. This relationship can be exploited in regions which contain examples of both pathways, but is complicated by additional factors such as water availability and air temperature. C3 plants fix carbon with the aid of the RuBisCO enzyme, from O_2 uptake and respiration of CO_2 from the leaves. Under low CO_2 regimes, C3 plants photosynthesize less and respire more, yielding a differential energy deficit under low CO_2. C4 plants however, convert carbon into diacid molecules prior to carbon fixation, which reduces the oxygen incorporation and augments the efficiency of carbon fixation, providing an advantage under low CO_2 concentrations. There is currently one record of biomarker $\delta^{13}C$ from the Bay of Bengal that has been used for CO_2 reconstruction extending back to ~1.5 million years before present (Yamamoto et al., 2022). That record overlaps and strongly correlates with ice core-derived CO_2, but prior to 800 kyrs the $\delta^{13}C$ tends to sit lower than other CO_2 proxies (including discontinuous ice samples), indicating there may be a calibration shift or regime change over the Mid-Pleistocene Transition or that other proxy groups are tending to overestimate CO_2 in the Early Pleistocene.

Modeling CO_2

There are two conceptually distinct ways in which models can be used to estimate past GHG changes: either using a carbon cycle model in conjunction with paleoceanographic reconstructions to project how much GHG might change, or use of a coupled climate-carbon cycle Earth System Model that includes all relevant internal feedbacks in conjunction with external forcing from Earth's orbit, ice sheet dynamics and geologic boundary conditions. That is, models can be used as a tool for the synthesis of diverse empirical reconstructions or as a tool to simulate our current understanding of what should have happened through the Quaternary (e.g., Yun et al., 2023) and the geologic past, or what may happen in the future.

Because it was evident from the ice core GHG reconstructions available since the 1980s that atmospheric CO_2 radiative forcing was the dominant GHG forcing over recent ice age climate cycles (See section "Ice core GHG reconstructions"; Fig. 4) more effort was invested into the modeling of past CO_2 changes than for the other GHGs.

One of the cornerstone questions in Earth System science is to "explain" why atmospheric CO_2 was lower during ice ages, as demonstrated by empirical evidence. What we seek is a quantitative attribution of the observed changes to distinct mechanistic explanations. The goal of this line of research is to identify which processes, dynamics and feedbacks were important in shaping the true history of Earth. As an example, non-GHG proxy records related to ocean circulation and the operation of the ocean's biological pump can be assimilated to project CO_2 changes in reasonably good agreement with empirical GHG reconstructions during the Mid Pleistocene, with the conclusion that the importance of dust-borne iron fertilization of the Southern Ocean as well as the Earth System sensitivity of climate to CO_2 radiative forcing both increased during this time of climate change (Chalk et al., 2017).

A second core question in Earth System science is to "explain" why Earth's climate changes through time, as demonstrated by empirical evidence. This question is of course directly related to the natural regulation of CO_2 in past atmospheres, but it is broader in the sense that it also addresses model projections of future climate and carbon cycle changes. The goal of this line of research is to identify a causal relationship in the coupled climate-carbon cycle system that can be used to project past or future climate and CO_2 change. As an example, slight but regular changes in the distribution of sunlight Earth receives each year caused by subtle changes in Earth's orbit around sun can account for much of the Quaternary climate record through a strong effect of orbit on ice sheets (Milankovitch, 1930) and subsequent indirect ice sheet effects on atmospheric CO_2 (Fig. 3).

Carbon dioxide as a driver of Quaternary climate

Geologic evidence for recurring cycles of climate change in the Quaternary period was first discovered in the 19th century, and scientific progress over the last two centuries has produced detailed reconstructions of periodic changes between cold "glacial" climate stages characterized by large ice sheets that covered parts of North America and Eurasia leading to lowered sea levels, and warm "interglacial" climate stages when northern ice sheets largely disappeared and sea levels were higher (Fig. 5). Over the last 10 thousand years Earth has been experiencing the Holocene period of interglacial conditions, and the Last Glacial Maximum (LGM) occurred as recently as 20 thousand years ago. These cycles of northern hemisphere glaciation (NHG) and glacial retreat intensified about 2.7 million years ago (intensification of NHG; iNHG) and the periodicity and severity of glacial/interglacial (G/IG) cycles increased again ~1 million years ago during the Mid Pleistocene Transition (MPT). The respective acronyms are in common use in Quaternary science.

Climate science has produced two contrasting frameworks to explain Quaternary climate change. One line of thought suggests external physical forcing causes a physical response in the climate system that yields the glacial/interglacial (G/IG) cycles. This category includes the Milankovitch theory that subtle periodic changes in Earth orbit influenced northern ice sheet advance and retreat (Milankovitch, 1930), which successfully predicts the 40-kyr periodicity found in Quaternary climate archives (Hays et al., 1976), as well as a number of tectonic, glaciologic or sea level-related hypotheses relevant to the iNHG and MPT. The other line of thought suggests that climate forcing from atmospheric CO_2 and other GHGs are responsible for much of the reconstructed Quaternary climate change, including a role in both iNHG and MPT (Lunt et al., 2008; Chalk et al., 2017). That is, Quaternary climate can be understood as the consequence of distinct physical forcings and mechanisms, or as the consequence of changes in atmospheric greenhouse gas levels related to global biogeochemical cycles (Yun et al., 2023). Quaternary climate science pursues the goal to reconcile these perspectives and thereby generate understanding of climate/carbon cycle feedbacks that are in play with ongoing anthropogenic Earth System change.

Northern Hemisphere glaciation

Extensive Northern Hemisphere Glaciation represents the culmination of a long-term Cenozoic cooling trend, and the start of the Quaternary period. Around 2.7 Ma ago (Ma, short for Myrs ago) glaciation of Greenland, North America, and Eurasia intensified leading to the 2.58 Ma transition from the Pliocene epoch of the Neogene period to the Pleistocene epoch of the Quaternary period (McClymont et al., 2023; Fig. 5). That is, the intensification of northern hemisphere glaciation (iNHG) yields the defining feature of the Pleistocene: substantial and regular bipolar glaciation. It is marked by an average of 1.5 ‰ increase in the oxygen isotope ratio of benthic foraminifera (Ahn et al., 2017), a global sea surface temperature decline of ~3 °C (Herbert et al., 2010) and the appearance of ice rafted debris in the North Atlantic and Pacific, commencing at ~2.5 Ma and ~2.7 Ma respectively. These dates are supported by the radiometric dating of till deposits on the North American continent (e.g., Balco and Rovey, 2010).

Theories for the iNHG broadly fall into two camps: Physical theories involving tectonic forcing causing a direct response of climate and/or ocean circulation, versus the crossing of a CO_2 climate threshold. During this interval uplift was occurring in both the Rocky Mountains and the Himalaya (although the majority of this uplift occurred during the Miocene), which have knock on effects for atmospheric circulation and increase the potential for chemical and physical weathering (Raymo and Ruddiman, 1992). Also during the Pliocene the shoaling of the Greenland Iceland Scotland Ridge and the closing of the isthmus of Panama have knock-on implications for the Atlantic meridional overturning circulation (AMOC) initiating or reinforcing the role it plays in ventilating the modern deep ocean (e.g., Haug and Tiedemann, 1998).

The contrasting theories suggest that the iNHG was caused by the radiative forcing from a reduction in atmospheric CO_2. More specifically, a long term declining trend in CO_2 since the Miocene may have reached a critical threshold in the climate system that allowed for bipolar glaciation and associated climate system feedbacks (Raymo and Ruddiman, 1992). More recently proxy evidence has been interpreted as a relatively abrupt reduction in atmospheric CO_2 aligned with the iNHG (Martínez-Botí et al., 2015; Bai et al., 2015). None of the currently available CO_2 proxy records for this interval are orbitally resolved, and thus the precise relationship of CO_2 to iNHG is unclear. The existing data (Lunt et al., 2008; Martínez-Botí et al., 2015) implies a decrease below 280 ppm CO_2 for the first time at ~2.7 Ma, which is a trigger point identified by several modeling studies. As such it seems plausible that tectonic forcing brought Earth to a threshold that resulted in coupled climate/carbon cycle feedbacks, thereby reconciling the contrasting physical and CO_2 centered hypotheses of the iNHG.

Mid-Pleistocene Transition

The Mid-Pleistocene Transition (MPT, ~800–1200 thousand years ago) marks a change in the Earth's orbitally paced ice age cycles, as they become longer, deeper (with colder maxima), and distinctly asymmetrical (saw-tooth shaped) from the broadly symmetrical cycles of the rest of the Pleistocene/Quaternary. The drivers behind and the feedbacks within this transition are not fully established, but the key orbital variability of Earth did not change (Imbrie et al., 1993). As with the iNHG, theories for the cause of the MPT are broadly defined by physical and CO_2-related arguments, with various degrees of intercompatibility between them.

The most prominent incumbent theory for the MPT involves the gradual removal of slippery regolith substrate during the early Quaternary, so as to expose the rigid cratonic bedrock which remains exposed today across the old footprint of the Laurentide ice sheet of North America, Fenoscandian ice sheet of Eurasia and other repeatedly glaciated areas. This theory invokes taller and more stable ice sheets appearing when basal friction increases due to progressive regolith (the soft sediment) removal, including the elevation/temperature feedback to stabilizing taller ice sheets (Clark and Pollard, 1998) but excluding any role for CO_2 or other GHG changes. Building further onto this argument, the lowering of sea level from larger northern hemisphere ice sheets could have allowed Antarctic ice sheets to expand onto the then exposed Antarctic shelf to produce a greater combined ice mass (Raymo and Huybers, 2008). These theories are supported by physical evidence of large-footprint Early Pleistocene ice sheets, even when compared to the Late Pleistocene (Balco and Rovey, 2010) alongside chemical evidence of lower total ice volumes prior to the MPT (Ahn et al., 2017). As such, the regolith removal hypothesis suggests a purely physical change that mediated the response of northern and subsequently southern ice sheets to stable cycles of orbital variability.

Recently proxy based reconstructions of atmospheric CO_2 have yielded evidence that GHG forcing also played a role in the MPT. High resolution CO_2 records from boron isotopes show a marked decline in CO_2 of glacial maxima over the transition, but no significant change in interglacial CO_2 (Chalk et al., 2017). These data implicate an ocean driven storage mechanism for additional glacial-stage CO_2 drawdown following the MPT, implicating a MPT strengthening in the dust-borne iron fertilization climate/carbon cycle feedback (Fig. 3; Martínez-Garcia et al., 2011). Less direct reconstruction of CO_2 by biomarker carbon isotopes argues for the opposite, that interglacial CO_2 increased over the MPT while glacials remained approximately consistent (Yamamoto et al., 2022). Blue ice measurements suggest an overall CO_2 decline, though the proportion of glacial-interglacial cycles captured is debatable in these snapshot archives (Yan et al., 2019).

Climate-CO_2 coupling of the Late Pleistocene

The continuous ice core GHG records of the last 800 kyr (See section "Ice core GHG reconstructions") reveal a stable relationship between global climate and atmospheric GHGs (Siegenthaler et al., 2005), where the implied GHG radiative forcing (>2 W/m^2) is sufficient to explain roughly half of the reconstructed GMT change over eight glacial/interglacial climate cycles. That is, since the MPT climate cycles stopped following the 40-kyr periodicity of orbital obliquity insolation forcing (Imbrie et al., 1992) and instead took on a distinct saw-tooth shape with an average period of about 100-kyr (Imbrie et al., 1993)–a new climate swing and rhythm that we now know perfectly matches radiative forcing from CO_2 and the other GHGs (Fig. 4). As such, if we accept GHG forcing as the proximal cause for late Pleistocene glacial/interglacial cycles the scientific problem shifts from explaining past climate change to explaining on a mechanistic level why CO_2 was lower during glacial periods; the "ice age CO_2 problem".

Temperature change, ice sheet mass, sea level change and GHG radiative forcing are all highly correlated throughout the late Pleistocene (Figs. 4 and 5), yielding two opposing views of the role of GHG: either ice age climate conditions are the result of physical climate changes that are amplified by positive carbon cycle feedbacks, or climate change forced by the carbon cycle is amplified by the positive ice/albedo feedbacks. Known carbon cycle responses to climate include both positive feedbacks such as temperature-dependence of CO_2 solubility in seawater or respiration rates of marine biomass, as well as negative feedbacks such as reduction in land carbon storage in a colder and drier climate or the reduction in ocean mass with expanding ice sheets.

However, available reconstructions of these feedbacks taken together fail to appreciably change atmospheric CO_2 (Hain and Sigman, 2024). For this reason, current hypotheses for glacial-stage CO_2 reductions are centered on changes in the ocean biological carbon storage driven by changes in deep water formation, deep ocean overturning circulation and CO_2 exchange between the polar ocean surface and the atmosphere, with the Southern Ocean at the nexus (Sigman et al., 2010). For example, more complete consumption of available nutrients by phytoplankton in the Southern Ocean surface would sequester additional carbon into the deep ocean, or an expansion of sea ice cover might prevent previously sequestered CO_2 from venting to the atmosphere (Stephens and Keeling, 2000). While there is expanding evidence that Southern Ocean nutrient consumption did increase during glacial stages (Sigman et al., 2021) and that deep ocean overturning did slow-down (Rafter et al., 2022), ocean general circulation models do not produce the prerequisite changes when forced with glacial climate conditions. Instead, these models tend to favor a glacial speeding-up of deep ocean overturning with sea ice expansion acting to reduce atmospheric CO_2. Either way, there is broad consensus that the polar ocean is critical to the regulation of late Pleistocene atmospheric CO_2.

Important additional constraints come from the timing of the relatively abrupt glacial termination following peak ice age conditions, which aligns with rising orbital obliquity (Huybers and Wunsch, 2005) but may require the presence of large unstable ice-sheets so that only every second or third obliquity cycle leads to glacial termination (Tzedakis et al., 2017). Further, deglacial CO_2 release was synchronous with warming during the termination of the last ice age cycle (Shakun et al., 2012), whereas the disintegration of the northern ice sheets and the attendant sea level rise lagged by millennia. As such, there is reason to believe that the modest orbital forcing of climate, ocean circulation and biological ocean carbon storage resulted in atmospheric CO_2 changes that principally caused the late Pleistocene climate cycles of gradual ice sheet growth followed by abrupt glacial termination. The physical trigger mechanism for abrupt ocean CO_2 release during glacial terminations is a key area of ongoing research.

Summary statement

We choose to highlight the contrast between purely physical mechanisms proposed to explain Quaternary climate change to those that involve the global carbon cycle and radiative climate forcing by changing atmospheric greenhouse gas concentrations (GHGs), not because we think of these perspectives as being in contrast but because they need to be aligned in order to unlock the potential of Quaternary climate science to inform our predictions of future climates and carbon cycles.

Orbital-timescale variability in Southern Ocean conditions are central to explaining observed GHG and climate variability of the late Pleistocene, and they are implicated as key drivers of both the iNHG that gave rise to the Quaternary period of bipolar glaciation as well as the MPT mode-change of glacial/interglacial climate cycles. As direct reconstructions of GHGs expand back in time to cover all of the Quaternary—and hopefully beyond—we have an opportunity to calibrate indirect methods to reconstruct climate/carbon cycle coupling even further back in time. This paleo work will provide new and novel challenges to the models we rely on to understand the carbon cycle and climate of today and the future.

References

Ahn S, Khider D, Lisiecki LE, and Lawrence CE (2017) A probabilistic Pliocene–Pleistocene stack of Benthic $\delta^{18}O$ using a profile hidden Markov Model. *Dynamics and Statistics of the Climate System* 2(1). https://doi.org/10.1093/climsys/dzx002.

Bai Y-J, Chen L-Q, Ranhotra PS, Wang Q, Wang Y-F, and Li C-S (2015) Reconstructing atmospheric CO_2 during the Plio–Pleistocene transition by fossil *Typha*. *Global Change Biology* 21(2): 874–881. https://doi.org/10.1111/gcb.12670.

Balco G and Rovey CW (2010) Absolute chronology for major Pleistocene advances of the Laurentide ice sheet. *Geology* 38(9): 795–798. https://doi.org/10.1130/G30946.1.

Bereiter B, Eggleston S, Schmitt J, Nehrbass-Ahles C, Stocker TF, Fischer H, Kipfstuhl S, and Chappellaz J (2015) Revision of the EPICA dome C CO $_2$ record from 800 to 600 Kyr before present. *Geophysical Research Letters* 42(2): 542–549. . https://doi.org/10.1002/2014GL061957.

Chalk TB, Hain MP, Foster GL, Rohling EJ, Sexton PF, Badger MPS, Cherry SG, et al. (2017) Causes of ice age intensification across the mid-Pleistocene transition. *Proceedings of the National Academy of Sciences* 114(50): 13114–13119. https://doi.org/10.1073/pnas.1702143114.

Clark PU and Pollard D (1998) Origin of the middle Pleistocene transition by ice sheet erosion of Regolith. *Paleoceanography* 13(1): 1–9. https://doi.org/10.1029/97PA02660.

De La Vega E, Chalk TB, Hain MP, Wilding MR, Casey D, Gledhill R, Luo C, Wilson PA, and Foster GL (2023) *Orbital CO_2 Reconstruction Using Boron Isotopes During the Late Pleistocene, An Assessment of Accuracy*. Preprint. Proxy Use-Development-Validation/Marine Archives/Pleistocene. . https://doi.org/10.5194/cp-2022-93.

Etminan M, Myhre G, Highwood EJ, and Shine KP (2016) Radiative forcing of carbon dioxide, methane, and nitrous oxide: A significant revision of the methane radiative forcing. *Geophysical Research Letters* 43(24). . https://doi.org/10.1002/2016GL071930.

Gottschalk J, Battaglia G, Fischer H, Frölicher TL, Jaccard SL, Jeltsch-Thömmes A, Joos F, et al. (2019) Mechanisms of millennial-scale atmospheric CO_2 change in numerical model simulations. *Quaternary Science Reviews* 220: 30–74. . https://doi.org/10.1016/j.quascirev.2019.05.013.

Hain MP and Sigman DM (2024) CO_2 in Earth's ice age cycles. In: *Oxford Research Encyclopedia of Climate Science*. Oxford, UK: Oxford University Press. In press.

Hain MP, Foster GL, and Chalk T (2018) Robust constraints on past CO_2 climate forcing from the boron isotope proxy. *Paleoceanography and Paleoclimatology* 33(10): 1099–1115. https://doi.org/10.1029/2018PA003362.

Haug GH and Tiedemann R (1998) Effect of the formation of the Isthmus of Panama on Atlantic Ocean thermohaline circulation. *Nature* 393(6686): 673–676. https://doi.org/10.1038/31447.

Hays JD, Imbrie J, and Shackleton NJ (1976) Variations in the Earth's orbit: Pacemaker of the ice ages: For 500,000 years, major climatic changes have followed variations in obliquity and precession. *Science* 194(4270): 1121–1132. https://doi.org/10.1126/science.194.4270.1121.

Herbert TD, Peterson LC, Lawrence KT, and Liu Z (2010) Tropical ocean temperatures over the past 3.5 million years. *Science* 328(5985): 1530–1534. https://doi.org/10.1126/science.1185435.

Hönisch B, et al. (2023) Towards a Cenozoic history of atmospheric CO_2. *Science*. https://doi.org/10.1126/science.adi5177.

Huybers P and Wunsch C (2005) Obliquity pacing of the Late Pleistocene glacial terminations. *Nature* 434(7032): 491–494. https://doi.org/10.1038/nature03401.

Imbrie J, Boyle EA, Clemens SC, Duffy A, Howard WR, Kukla G, Kutzbach J, et al. (1992) On the structure and origin of major glaciation cycles 1. Linear responses to Milankovitch forcing. *Paleoceanography* 7(6): 701–738. . https://doi.org/10.1029/92PA02253.

Imbrie J, Berger A, Boyle EA, Clemens SC, Duffy A, Howard WR, Kukla G, et al. (1993) On the structure and origin of major glaciation cycles 2. The 100,000-year cycle. *Paleoceanography* 8(6): 699–735. . https://doi.org/10.1029/93PA02751.

Intergovernmental Panel on Climate Change (2023) *Climate Change 2021—The Physical Science Basis: Working Group I Contribution to the Sixth Assessment Report of the Intergovernmental Panel on Climate Change*, 1st edn. Cambridge University Press. https://doi.org/10.1017/9781009157896.

Loulergue L, Schilt A, Spahni R, Masson-Delmotte V, Blunier T, Lemieux B, Barnola J-M, Raynaud D, Stocker TF, and Chappellaz J (2008) Orbital and millennial-scale features of atmospheric CH_4 over the past 800,000 years. *Nature* 453(7193): 383–386. . https://doi.org/10.1038/nature06950.

Lunt DJ, Foster GL, Haywood AM, and Stone EJ (2008) Late Pliocene greenland glaciation controlled by a decline in atmospheric CO_2 levels. *Nature* 454(7208): 1102–1105. https://doi.org/10.1038/nature07223.

Martínez-Botí MA, Foster GL, Chalk TB, Rohling EJ, Sexton PF, Lunt DJ, Pancost RD, Badger MPS, and Schmidt DN (2015) Plio-Pleistocene climate sensitivity evaluated using high-resolution CO_2 records. *Nature* 518(7537): 49–54. . https://doi.org/10.1038/nature14145.

Martínez-Garcia A, Rosell-Melé A, Jaccard SL, Geibert W, Sigman DM, and Haug GH (2011) Southern ocean dust–climate coupling over the past four million years. *Nature* 476(7360): 312–315. . https://doi.org/10.1038/nature10310.

McClymont EL, Ho SL, Ford HL, Bailey I, Berke MA, Bolton CT, De Schepper S, et al. (2023) Climate evolution through the onset and intensification of northern hemisphere glaciation. *Reviews of Geophysics* 61(3): e2022RG000793. . https://doi.org/10.1029/2022RG000793.

Milankovitch M (1930) Mathematische Klimalehre Und Astronomische Theorie Der Klimaschwankungen. In: *Allgemeine Klimalehre. Handbuch Der Klimatologie*, Vol. 1. Berlin: Borntraeger.

Rae JWB (2018) Boron isotopes in foraminifera: Systematics, biomineralisation, and CO_2 reconstruction. In: Marschall H and Foster G (eds.) *Boron Isotopes. Advances in Isotope Geochemistry*, pp. 107–143. Cham: Springer International Publishing. . https://doi.org/10.1007/978-3-319-64666-4_5.

Rafter PA, Gray WR, Hines SKV, Burke A, Costa KM, Gottschalk J, Hain MP, et al. (2022) Global reorganization of deep-sea circulation and carbon storage after the last ice age. *Science Advances* 8(46): eabq5434. . https://doi.org/10.1126/sciadv.abq5434.

Raymo ME and Huybers P (2008) Unlocking the mysteries of the ice ages. *Nature* 451(7176): 284–285. . https://doi.org/10.1038/nature06589.

Raymo ME and Ruddiman WF (1992) Tectonic forcing of late Cenozoic climate. *Nature* 359(6391): 117–122. . https://doi.org/10.1038/359117a0.

Schilt A, Baumgartner M, Blunier T, Schwander J, Spahni R, Fischer H, and Stocker TF (2010) Glacial–interglacial and millennial-scale variations in the atmospheric nitrous oxide concentration during the last 800,000 years. *Quaternary Science Reviews* 29(1–2): 182–192. . https://doi.org/10.1016/j.quascirev.2009.03.011.

Shakun JD, Clark PU, He F, Marcott SA, Mix AC, Liu Z, Otto-Bliesner B, Schmittner A, and Bard E (2012) Global warming preceded by increasing carbon dioxide concentrations during the last deglaciation. *Nature* 484(7392): 49–54. . https://doi.org/10.1038/nature10915.

Sherwood SC, Webb MJ, Annan JD, Armour KC, Forster PM, Hargreaves JC, Hegerl G, et al. (2020) An assessment of Earth's climate sensitivity using multiple lines of evidence. *Reviews of Geophysics* 58(4): e2019RG000678. . https://doi.org/10.1029/2019RG000678.

Siegenthaler U, Stocker TF, Monnin E, Luthi D, Schwander J, Stauffer B, Raynaud D, et al. (2005) Stable carbon cycle–climate relationship during the late Pleistocene. *Science* 310: 6.

Sigman DM, Hain MP, and Haug GH (2010) The Polar Ocean and glacial cycles in atmospheric CO_2 concentration. *Nature* 466(7302): 47–55. . https://doi.org/10.1038/nature09149.

Sigman DM, Fripiat F, Studer AS, Kemeny PC, Martínez-García A, Hain MP, Ai X, Wang X, Ren H, and Haug GH (2021) The Southern Ocean during the Ice ages: A review of the Antarctic surface isolation hypothesis, with comparison to the North Pacific. *Quaternary Science Reviews* 254: 106732. . https://doi.org/10.1016/j.quascirev.2020.106732.

Snyder CW (2016) Evolution of global temperature over the past two million years. *Nature* 538(7624): 226–228. . https://doi.org/10.1038/nature19798.

Stap LB, De Boer B, Ziegler M, Bintanja R, Lourens LJ, and Van De Wal RSW (2016) CO_2 over the past 5 million years: Continuous simulation and new δ^{11} B-based proxy data. *Earth and Planetary Science Letters* 439: 1–10. . https://doi.org/10.1016/j.epsl.2016.01.022.

Stephens BB and Keeling RF (2000) The influence of Antarctic sea ice on glacial–interglacial CO_2 variations. *Nature* 404(6774): 171–174. . https://doi.org/10.1038/35004556.

Trenberth KE, Fasullo JT, and Kiehl J (2009) Earth's global energy budget. *Bulletin of the American Meteorological Society* 90(3): 311–324. . https://doi.org/10.1175/2008BAMS2634.1.

Tzedakis PC, Crucifix M, Mitsui T, and Wolff EW (2017) A simple rule to determine which insolation cycles lead to interglacials. *Nature* 542(7642): 427–432. . https://doi.org/10.1038/nature21364.

Van De Wal RSW, De Boer B, Lourens LJ, Köhler P, and Bintanja R (2011) Reconstruction of a continuous high-resolution co$_2$ record over the past 20 million years. *Climate of the Past* 7(4): 1459–1469. . https://doi.org/10.5194/cp-7-1459-2011.

Walker JCG, Hays PB, and Kasting JF (1981) A negative feedback mechanism for the long-term stabilization of Earth's surface temperature. *Journal of Geophysical Research: Oceans* 86(C10): 9776–9782. . https://doi.org/10.1029/JC086iC10p09776.

Yamamoto M, Clemens SC, Seki O, Tsuchiya Y, Huang Y, O'ishi R, and Abe-Ouchi A (2022) Increased interglacial atmospheric CO_2 levels followed the mid-Pleistocene transition. *Nature Geoscience* 15(4): 307–313. . https://doi.org/10.1038/s41561-022-00918-1.

Yan Y, Bender ML, Brook EJ, Clifford HM, Kemeny PC, Kurbatov AV, Mackay S, et al. (2019) Two-million-year-old snapshots of atmospheric gases from Antarctic Ice. *Nature* 574(7780): 663–666. . https://doi.org/10.1038/s41586-019-1692-3.

Yun K-S, Timmermann A, Lee S-S, Willeit M, Ganopolski A, and Jadhav J (2023) A transient coupled general circulation model (CGCM) simulation of the past 3 million years. *Climate of the Past* 19(10): 1951–1974. https://doi.org/10.5194/cp-19-1951-2023.

Zhang YG, Pearson A, Benthien A, Dong L, Huybers P, Liu X, and Pagani M (2019) Refining the alkenone-pCO_2 method I: Lessons from the Quaternary glacial cycles. *Geochimica et Cosmochimica Acta* 260: 177–191. . https://doi.org/10.1016/j.gca.2019.06.032.

Zhong W and Haigh JD (2013) The greenhouse effect and carbon dioxide. *Weather* 68(4): 100–105. https://doi.org/10.1002/wea.2072.